Soft Matter

PAPER

View Article Online
View Journal | View Issue

Open Access Article. Published on 22 August 2024. Downloaded on 1/20/2026 11:14:46 PM.
This article is licensed under a Creative Commons Attribution 3.0 Unported Licence.

Check for updates

Cite this: *Soft Matter*, 2024, **20**, 7133

Flow of wormlike micellar solutions over concavities†

Fabian Hillebrand, *[a] Stylianos Varchanis, [ab] Cameron C. Hopkins, [a] Simon J. Haward [a] and Amy Q. Shen [a]

Received 17th May 2024,
Accepted 19th August 2024

DOI: 10.1039/d4sm00594e

rsc.li/soft-matter-journal

We present a comprehensive investigation combining numerical simulations with experimental validation, focusing on the creeping flow behavior of a shear-banding, viscoelastic wormlike micellar (WLM) solution over concavities with various depths (D) and lengths (L). The fluid is modeled using the diffusive Giesekus model, with model parameters set to quantitatively describe the shear rheology of a 100 : 60 mM cetylpyridinium chloride:sodium salicylate aqueous WLM solution used for the experimental validation. We observe a transition from "cavity flow" to "expansion–contraction flow" as the length L exceeds the sum of depth D and channel width W. This transition is manifested by a change of vortical structures within the concavity. For $L \leq D + W$, "cavity flow" is characterized by large scale recirculations spanning the concavity length. For $L > D + W$, the recirculations observed in "expansion–contraction flow" are confined to the salient corners downstream of the expansion plane and upstream of the contraction plane. Using the numerical dataset, we construct phase diagrams in L–D at various fixed Weissenberg numbers Wi, characterizing the transitions and describing the evolution of vortical structures influenced by viscoelastic effects.

1 Introduction

Viscoelastic fluids are encountered in a variety of different flow configurations specifically within manufacturing processes, such as during fiber spinning, extrusion, or for drag reduction. To better understand the flow of such fluids, numerous experimental and numerical studies have been performed for a variety of geometries encountered in manufacturing processes, such as for expansion flows,[1–3] contraction flows,[4–10] contraction–expansion flows,[11–17] or flows past concavities[17–22] (*e.g.*, see Fig. 1). All of these geometries introduce salient and re-entrant corners to the flow as well as changes in the cross-section. These result in complex flow structures for viscoelastic fluids such as lip vortices, corner vortices, or time-dependence even at negligible inertia. Due to this, these simple geometries are also used as benchmarks for numerical methods with non-Newtonian constitutive models,[23] with specifically the 4-1 contraction channel garnering significant attention. Another similar benchmark is the lid-driven cavity,[24–27] which is used extensively for inertial flows.[28–30] For viscoelastic fluids, the effect of changing the aspect ratio (depth-to-length) of the lid-driven cavity has been investigated both experimentally[31,32] and numerically.[33] However, while a number of studies consider the

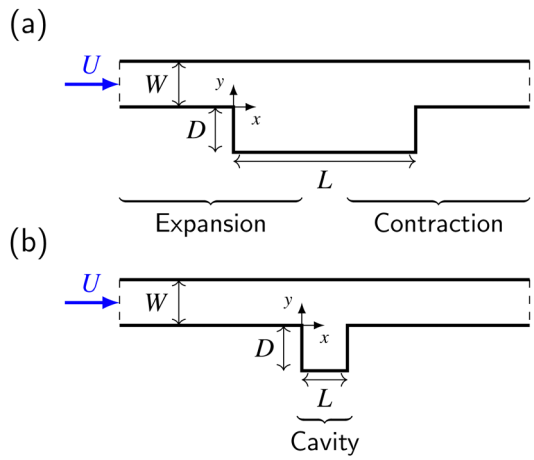

Fig. 1 Examples of fluidic channels with a concavity on one wall, where W is the width of the channel, and D and L are the depth and length of the concavity, respectively. For $L \gg D$, we refer to the concavity as a (one-sided) "expansion–contraction" (a). For $L \lesssim D$, we refer to the concavity simply as a "cavity" (b). In each case the coordinate system is indicated with origin at the re-entrant corner of the expansion plane. In experiments we also define the uniform height H of the geometry through the z-direction (out of the page).

[a] Micro/Bio/Nanofluidics Unit, Okinawa Institute of Science and Technology Graduate University, Onna-son, Kunigami-gun, Okinawa 904-0495, Japan. E-mail: fabian.hillebrand@oist.jp

[b] Center for Computational Biology, Flatiron Institute, Simons Foundation, New York, NY 10010, USA

† Electronic supplementary information (ESI) available. See DOI: https://doi.org/10.1039/d4sm00594e

Open Access Article. Published on 22 August 2024. Downloaded on 1/20/2026 11:14:46 PM.
This article is licensed under a Creative Commons Attribution 3.0 Unported Licence.

effect of changing the dimensions for expansion, contraction, or lid-driven cavity flows,[3,8,20,34–36] it is not entirely clear how the flow of a viscoelastic fluid over a concavity transitions from "expansion–contraction flow" to "cavity flow" (Fig. 1). Here we consider the flow over different concavities to investigate this transition.

We focus on flows of entangled wormlike micellar (WLM) solutions. WLMs are formed from surfactants that self-organize into elongated micellar chains often termed "living polymers",[37–40] distinguishing them from conventional polymers as they possess the ability to reform after breaking. This is particularly relevant for flows with large elastic stresses and results in elastic instabilities absent in polymer solutions,[41] and for strong flows that result in breaking of the micelles.[42–49] New elastic instabilities also include interface instabilities and jetting exhibited for channels with high aspect ratios.[50–52] WLM solutions find varied applications, serving as drag reduction agents in industrial settings and as rheological modifiers in household products.[53–56] They are further renowned to be strongly shear-thinning and even to display shear-banding phenomena. Shear-banding, or gradient banding, is characterized by multiple distinct shear rates that correspond to the same shear stress value, forming in practice a plateau in shear stress.[57,58]

In addition to strong shear-thinning and shear-banding, WLM solutions also exhibit memory effects, which are associated with a relaxation time λ that Newtonian fluids lack. They maintain a memory of their past states due to their internal structure and interactions. This introduces a temporal aspect to their behavior, influencing various flow processes and material behaviors. To quantify these effects we use the non-dimensional Weissenberg number Wi, defined as the product of λ and a characteristic shear-rate $\dot{\gamma}$, with the latter typically estimated by a characteristic velocity and length scale. In this study, we use the mean velocity U and channel width W upstream of the expansion plane or, equivalently, downstream of the contraction plane, see Fig. 1:

$$\mathrm{Wi} = \frac{\lambda U}{W}. \tag{1}$$

The Weissenberg number Wi provides a measure of viscoelasticity and can be interpreted as the dimensionless ratio of elastic to viscous forces.[59,60] Additionally, given that the Weissenberg number is inversely proportional to the length scale W, its value tends to increase significantly in systems with small length scales, given the same relaxation time λ and mean velocity U. On the other hand, inertial effects scale as proportional to the length scale, thus making microfluidics the ideal platform to study elastic effects with negligible inertia.

WLM solutions have been experimentally studied in various geometries at small scales,[42,61] including the cross-slot,[62–64] the flow around a sharp bend,[65,66] contraction–expansion or contraction flows,[67–70] as well as over concavities,[34] though not necessarily in the shear-banding regime. These studies typically describe lip vortices upstream of re-entrant corners, corner vortices within salient corners, and unsteady flow depending on Wi. Similarly, numerical works have been performed using various constitutive models to capture the flow behavior of WLM solutions in contraction–expansion,[71] contraction,[72,73] or expansion–contraction flows.[74–76] It should be mentioned that unlike for Newtonian flows, where the Newtonian law of viscosity is well-established, modeling complex fluids is a difficult task even under low or negligible inertial effects and typically leads to only a semi-quantitative prediction.[23,77] A recent study by Varchanis *et al.*[78] suggests that the Giesekus constitutive model,[79] although not initially developed for wormlike micelles, is the most suitable model among the ones considered for shear-banding WLM solutions, offering the closest qualitative match to experimental observations. However, similar to the other models examined (including the Johnson–Segalmann model[80] and Vasquez–Cook–McKinley model[81]), the Giesekus model can only provide quantitative agreements for a limited range of flow conditions. Additionally, previous studies have highlighted certain shortcomings of the Giesekus model, particularly in its treatment of time dependence.[82]

In this study, we investigate the flow behavior of a viscoelastic WLM solution over a geometric configuration with a concavity by considering the transition from one-sided expansion–contractions to narrow cavities as we vary D and L (Fig. 1). We primarily use numerical simulations with the diffusive Giesekus model to investigate this transition, complemented by comparisons with microfluidic experiments on expansion–contraction flows. In Section 2 we detail our methodology, including the experimental procedures, the governing equations, and the numerical frameworks. We discuss our results in Section 3, starting by comparing experiment and simulation with an emphasis on the expansion phase, followed by a discussion on the simulations and exhibited flow structures as we decrease the length L with respect to the depth D. We end the section by summarizing the observations in phase diagrams at selected Wi values. Finally, Section 4 concludes our study with an outlook for future studies.

2 Methods

2.1 Experiments

2.1.1 Sample preparation. The test fluid employed for experimental validation of our comprehensive numerical study is a very widely used WLM solution consisting of 100 mM cetylpyridinium chloride (CpyCl) and 60 mM sodium salicylate (NaSal) dissolved in Milli-Q water.[78,83,84] The solution is identical to that used by Hopkins *et al.*,[85] where the fluid rheology is measured at 24 °C with a DHR3 stress-controlled rotational rheometer (TA Instruments Inc.) fitted with a 40 mm diameter, 1° angle cone-and-plate geometry. The rheological properties are determined by fitting the measured fluid rheology to the Giesekus model, see Fig. 2 and Section 2.2. The fit to the flow curve in Fig. 2(a) yields the zero-shear viscosity $\eta_0 = \eta_p + \eta_s$, where η_p and η_s are the polymer and solvent viscosity in the Giesekus model, respectively, and infinite shear viscosity $\eta_\infty \equiv \eta_s$. We find the relaxation time λ = 1.54 s from the analytic solution of the Giesekus model, which matches the single-mode Maxwell model with a viscous contribution:

$$G'(\omega) = \frac{G_0\lambda^2\omega^2}{1+\lambda^2\omega^2}, \quad G''(\omega) = \frac{G_0\lambda\omega}{1+\lambda^2\omega^2} + \eta_s\omega, \tag{2}$$

 This journal is © The Royal Society of Chemistry 2024

Open Access Article. Published on 22 August 2024. Downloaded on 1/20/2026 11:14:46 PM.
This article is licensed under a Creative Commons Attribution 3.0 Unported Licence.

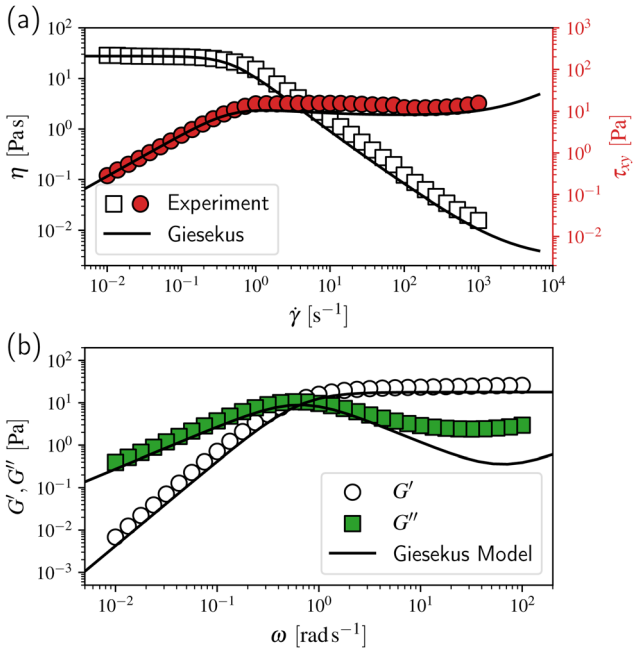

Fig. 2 Comparison between experimental (T = 24 °C)[85] and simulated rheological data using the Giesekus model for (a) simple shear and (b) small amplitude oscillatory shear. For small amplitude oscillatory shear, the Giesekus model matches the single-mode Maxwell model complemented with a viscous contribution $\eta_s\omega$ for the loss modulus, see eqn (2). We use the material parameters λ = 1.54 s and $G_0 = \eta_0/\lambda$ for the simulation.

where $G'(\omega)$ is the storage modulus, $G''(\omega)$ the loss modulus, G_0 the plateau modulus, and ω the frequency. The plateau modulus obtained from the fitting is $G_0 = \eta_0/\lambda \approx 17.9$ Pa. The experimental data are compared with the predicted values from the Giesekus model in Fig. 2(b). Note that at high frequencies the Giesekus model deviates from the experimental data. This is due to a trade-off as the Giesekus model cannot fit both the simple shear and the small amplitude oscillatory shear data simultaneously. For more details on the experimental fluid, including a detailed solution preparation, see ref. 85.

2.1.2 Experimental setup. Fig. 1 illustrates the key dimensions of the channels, where in the experiments the width W and height H are fixed at 0.8 mm and 3 mm, respectively. For the direct comparison with simulations we use a device with $D = W$ and $L = 5W$ which will correspond to an expansion–contraction configuration. Two additional devices, also expansion–contraction configurations, with $D = 1.5W$ and $L = 10W$ as well as $D = 2W$ and $L = 10W$, are used in the ESI.† The microfluidic devices are fabricated from a solid fused silica glass substrate using a subtractive manufacturing technique based on selective laser-induced etching.[86] Polytetrafluoroethylene (PTFE) tubing is then attached to the microfluidic device using two-part epoxy and Musashi double-thread syringe tips. The PTFE tubing is relatively rigid and is used to minimize the effects of tube compliance on the fluid flow. The flow is driven by a low-pressure Nemesys pump system (Cetoni GmbH) equipped with 25 mL Hamilton Gastight glass syringes. We impose equal and opposite volumetric flow rates Q at the inlet and outlet of the microchannel. The characteristic velocity is calculated as $U = Q/wH$.

Experimental velocity fields are obtained using microparticle image velocimetry (μ-PIV). The test fluid is seeded with a low concentration (≈0.02 wt%) of 2 μm-diameter fluorescent tracers (Thermo Fisher), with an excitation wavelength of 530 nm and emission wavelength of 607 nm. We use Insight 4G™ software (TSI Inc.) together with a Phantom Miro M310 high-speed camera and a Nikon Eclipse Ti inverted optical microscope with a 4× magnification (Nikon Plan Fluor objective lens, numerical aperture NA = 0.13) to record PIV frame pairs. The focal plane is set at the half-height of the channel. For the tracer particles to fluoresce we use volume illumination *via* an Nd:YLF dual-pulsed laser with a wavelength of 527 nm. The time between laser pulses is chosen such that the displacement of tracer particles between the two images in each pair is around 4 pixels. After letting the flow stabilize for 20–60 s (depending on the imposed flow rate), a total of 500 image pairs are captured at a rate of 50 frames-per-second. Cross-correlation and post-processing of the raw PIV frame pairs is performed with OpenPIV[87] in Python.

2.2 Governing equations

We assume that the flow is governed by the incompressible and isothermal Cauchy equations coupled with the diffusive Giesekus constitutive model that accounts for the viscoelastic stresses. Neglecting inertia, the continuity and momentum equations read:

$$\nabla\cdot\mathbf{u} = 0, \tag{3}$$

$$\nabla\cdot(-p\mathbf{I} + \boldsymbol{\tau} + \eta_s\dot{\boldsymbol{\gamma}}) = \mathbf{0}, \tag{4}$$

where p is the thermodynamic pressure, $\mathbf{I}$ is the identity tensor, $\boldsymbol{\tau}$ is the viscoelastic contribution to the total stress tensor, $\dot{\boldsymbol{\gamma}} = \nabla\mathbf{u} + \nabla\mathbf{u}^{\mathrm{T}}$ is the deformation rate tensor (or twice the symmetric velocity gradient), and η_s is the solvent viscosity. The diffusive Giesekus constitutive model is expressed in the stress tensor formulation as follows:

$$\lambda\overset{\nabla}{\boldsymbol{\tau}} + \boldsymbol{\tau} + \frac{\alpha\lambda}{\eta_p}\boldsymbol{\tau}\cdot\boldsymbol{\tau} = \eta_p\dot{\boldsymbol{\gamma}} + \lambda D_s\nabla^2\boldsymbol{\tau}, \tag{5}$$

where λ is the relaxation time, α is the mobility parameter, η_p is the polymer viscosity, and D_s is the stress diffusion coefficient. The first term denotes the upper convected derivative of the viscoelastic stress tensor:

$$\overset{\nabla}{\boldsymbol{\tau}} = \frac{\partial\boldsymbol{\tau}}{\partial t} + \mathbf{u}\cdot\nabla\boldsymbol{\tau} - \nabla\mathbf{u}^{\mathrm{T}}\cdot\boldsymbol{\tau} - \boldsymbol{\tau}\cdot\nabla\mathbf{u}. \tag{6}$$

The presence of the stress diffusion term[88] in the constitutive eqn (5) is necessary because it provides a smooth transition between the shear bands and the uniqueness of the numerical solution when the flow is shear-banded.[89]

We further define the mean squared velocity over the simulation domain Ω as:

$$\langle u^2\rangle = \frac{1}{|\Omega|}\int_\Omega u^2\mathrm{d}\Omega, \tag{7}$$

where $u = \|\mathbf{u}\|$ is the velocity magnitude and $|\Omega|$ is the size of

Open Access Article. Published on 22 August 2024. Downloaded on 1/20/2026 11:14:46 PM.
This article is licensed under a Creative Commons Attribution 3.0 Unported Licence.

the simulation domain Ω. Similarly, we define the total elastic Helmholtz free energy[90,91] as:

$$F_{\mathrm{el}} = \frac{1}{2}\int_{\Omega} \mathrm{tr}(\boldsymbol{\tau})\mathrm{d}\Omega - \frac{1}{2}\int_{\Omega} \frac{\eta_{\mathrm{p}}}{\lambda} \log\det\left(\frac{\lambda}{\eta_{\mathrm{p}}}\boldsymbol{\tau} + \mathbf{I}\right)\mathrm{d}\Omega. \tag{8}$$

The elastic Helmholtz free energy $F_{\mathrm{el}} = E_{\mathrm{el}} - TS$ consists of two contributions. The first contribution is the elastic potential energy E_{el} consisting of the trace of the viscoelastic stress tensor $\boldsymbol{\tau}$. It is associated with an internal entropy when the internal microstructures are viewed as ideal polymeric chains.[91,92] The second contribution is the entropy contribution S of the entire system at temperature T and uses the logarithm and determinant, corresponding to the number of microstates. This term corrects the available energy for isothermal systems.[91,93]

The model parameters of the Giesekus model (see Table 1) are calculated by fitting the predictions of the model in simple shear and small amplitude oscillatory shear using the experimental data discussed already in Section 2.1.1 and is shown in Fig. 2. Fielding and coworkers gave a simple and efficient rule for choosing the stress diffusion D_{s} in numerical simulations:[82,94] $\sqrt{\lambda D_{\mathrm{s}}} \approx 10^{-2}W$. This rule is based on the interface width between the shear bands that scales as $O\left(\sqrt{\lambda D_{\mathrm{s}}}\right)$. With respect to our experiments, with a channel width of $W = 8 \times 10^{-4}$ m and a relaxation time of $\lambda = 1.54$ s, we find a value of $D_{\mathrm{s}} \approx 4 \times 10^{-11}$ m^2 s^{-1}. For numerical stability, we relax this value to $D_{\mathrm{s}} = 4 \times 10^{-10}$ m^2 s^{-1}. This stress diffusion coefficient lies within the range of experimental measurements for similar WLM solutions[58,95–102] and thus we expect the difference to Fielding and coworkers' rule to be negligible. Moreover, we note that in the simulations the corresponding interface width, assuming the flow is fully shear-banded, corresponds to $\approx 0.04W$, which is discussed further in the ESI,† Section S1. For short ($L \ll W$) and shallow ($D \ll W$) geometries the interface width is expected to influence the flow.[99] The experimental value, see again Section S1 (ESI†), appears to be around $0.07W$, though this estimate is affected by numerous sources of noise. Nevertheless, we in fact see that, although increased for numerical stability, the larger stress diffusion is potentially more appropriate for our experimental fluid. We note that the interface width appears to be relatively large compared to the channel width. Therefore, the shear-banding nature of the fluid in our geometry is not entirely established and as such we will typically refer to shear localization, referring to the region of high shear between low shear regions or near the wall, rather than shear bands.

Table 1 Parameters of the diffusive Giesekus model (5) in dimensional and non-dimensional form, with the latter here denoted with a superscript "*"

η_{p} [Pa s]	η_{s} [Pa s]	λ [s]	α	D_{s} [m^2 s^{-1}]
27.5	2.75×10^{-3}	1.54	0.85	4×10^{-10}
η_p^*	η_s^*	λ^*	α^*	D_s^*
1–10^{-4}	10^{-4}	Wi	0.85	10^{-3}

The eqn (3)–(5) are solved in their non-dimensional form using as scaling quantities the characteristic mean velocity U, characteristic channel width W, the zero-shear viscosity $\eta_0 = \eta_{\mathrm{p}} + \eta_{\mathrm{s}}$, and the flow time scale W/U (see Fig. 1 and Table 1).

2.3 Simulations

The coupled non-linear eqn (3)–(5), restricted to two dimensions, are solved using the Petrov–Galerkin stabilized finite element method for viscoelastic flows (PEGAFEM-V) developed by Varchanis *et al.*[27,103,104] Linear basis functions are used together with the Newton-Raphson method to solve the system of non-linear equations. In total, we have 6 unknown quantities at each node of the numerical mesh (Fig. 3), corresponding to the pressure p, the velocity $\mathbf{u}$, and the symmetric stress tensor $\boldsymbol{\tau}$. We use steady-state simulations to explore Wi ranging from 0.1 to 30 but separately verify steadiness using a time-dependent simulation with 2nd-order backward finite differences and a time-step $\Delta t = 0.01$ at fixed Wi values starting from a zero initial state. In particular, we only probe a limited set of Wi values and assume that once a flow becomes unsteady, it will not return to steady flow for higher Wi values. This is motivated by our experimental observations. When the time-dependent simulation converge to a steady-state, they appear identical to the steady-state simulations when the two are compared. We note that according to Moorcroft and Fielding,[82] we generally expect discrepancies relating to time dependence for the Giesekus model. In general, we expect only a qualitative, not quantitative, agreement with respect to experiments.

We employ the usual no-slip and no-penetration boundary conditions (*i.e.*, $\mathbf{u} = \mathbf{0}$) on all walls. Furthermore, we enforce no-flux through the walls for the stress (*i.e.*, $\mathbf{n}\cdot\nabla\boldsymbol{\tau} = \mathbf{0}$).[58,105] At the inlet, we impose fully developed velocity and stress fields, while we apply the open boundary condition (OBC)[106] at the outlet. In all simulations we use structured meshes composed of linear triangular elements. The mesh density is higher near the walls and within the cavity, where the largest elements have a

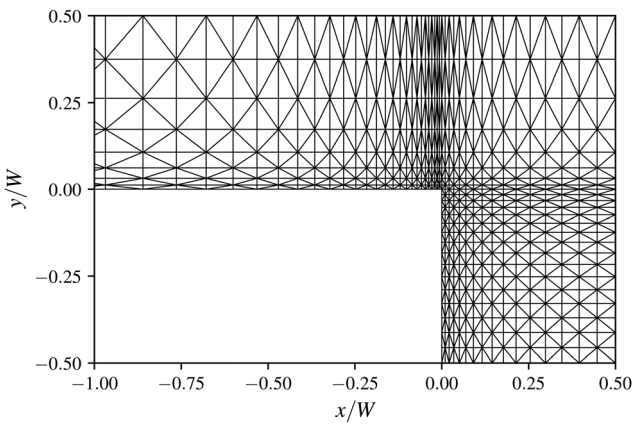

Fig. 3 Schematic of the mesh around the upstream re-entrant corner illustrating the different densities of the elements ($D = W$, $L = W$). Shown is a coarse mesh created only for visualization purposes and not for simulations. The total number of elements is 6144 compared to the actual mesh used with 393 216 elements.

Open Access Article. Published on 22 August 2024. Downloaded on 1/20/2026 11:14:46 PM.
This article is licensed under a Creative Commons Attribution 3.0 Unported Licence.

maximum size of $10^{-2}W$. Near the walls, the elements have a width in wall-direction of $\lesssim 2 \times 10^{-3}W$ to account for shear localization. This value is consistent with the experimental interface width, which is of the order $10^{-2}W$. A schematic of the mesh around the expansion re-entrant corner is shown in Fig. 3 for a square cavity. The actual mesh used for the geometry has 64 times more elements. The total number of elements ranges between approximately 400 000 and 4 000 000, accounting for the different concavity sizes. In the ESI,† Section S2 we consider the effect of mesh size on $\langle u^2 \rangle$ and E_{el} for the cavity with $D = W$ and $L = W$. The accuracy of the numerical solution decreases with increasing Wi due to shear localization occurring within the bulk, acting as a primary limiting factor for the simulations. This happens because sharp variations in the deformation rate occur within the region of shear localization. We further expect a nearly singular point at the re-entrant corner.[107] Due to this, we repeat our simulations with a mesh where the re-entrant corners are smoothed using a quarter circle with radius $2 \times 10^{-2}W$, but no significant change is observed for the flow structures inside the concavity, as discussed in the ESI,† Section S3.

In some cases, the simulation fails to converge, potentially due to issues related to the interface width and/or the mesh resolution. Alternatively, the simulations may also fail due to subcritical behaviors that the first order continuation, corresponding to an equal spacing in Wi, cannot resolve. To handle such cases, we use the pseudo-arclength continuation[108,109] for advancing in Wi. In this method, an auxiliary problem is solved for the solution vector $\mathbf{T}$, which consists of all unknown quantities at each node including the current Wi value. The solution vector follows a trajectory in the solution space which is parameterized by the pseudo-arclength s. At step $n + 1$ with step size Δs, the solution vector is updated by solving the auxiliary equation:

$$\dot{\mathbf{T}}_n \cdot (\mathbf{T}_{n+1} - \mathbf{T}_n) = \Delta s, \tag{9}$$

where $\mathbf{T}_n$ and $\dot{\mathbf{T}}_n$ are the point and tangent of the trajectory at the previous step n, respectively, together with the eqn (3)–(5). The step size Δs is adaptively updated based on the error in the prediction. While the pseudo-arclength continuation works exceptionally well, it also allows convergence in cases where mesh resolution is clearly insufficient. Where possible, we use a single mesh refinement to verify if a seemingly critical behavior, in particular, multi-valued solutions at a given Wi value, is qualitatively retained. Nevertheless, there are some questions about the validity of these numerical solutions, see also the ESI,† Section S5.

3 Results and discussion

For validation purposes, we begin our presentation of the results with a brief comparison between simulation and experiment. Subsequently, we consider the mean squared velocity and elastic Helmholtz free energy derived from the numerical simulations as a function of Wi. Next, we present the bulk of our detailed numerical simulations, beginning with expansion–contraction flows and proceeding by decreasing the length L relative to the depth D until we reach cavity flows. Finally, we summarize our results and provide phase diagrams in D and L at fixed Wi.

3.1 Comparison to experiment

For the comparison between experimental and simulated data, we focus on the expansion phase in the expansion–contraction regime. In Fig. 4(a) and (b) we show the velocity magnitude u and streamlines for the microchannel with $D = W$ and $L = 5W$ at Wi = 1 and Wi = 5. A good qualitative match is found with their corresponding simulations, shown in Fig. 4(c) and (d), respectively. In particular, in both the experiment and the simulation at Wi = 5 (Fig. 4(b) and (d)), we note the formation of lip and corner vortices at the re-entrant and salient corners upstream and downstream of the expansion plane, respectively. For the experiment at Wi = 5 a quantitatively better match in terms of vortex sizes is obtained for a higher Wi = 30 in the simulation, see Fig. 4(e). This again demonstrates that the diffusive Giesekus model only captures the flow qualitatively and some quantitative deviations are expected. Nevertheless, we note that all flow structures as well as their Wi dependence are captured by the simulations.

A detailed discussion on the lip vortex is provided in the ESI,† Section S4, with a quantitative comparison for the lip vortex sizes between experiment and simulation in Section S4.1 (ESI†). In the next section we consider the mean squared

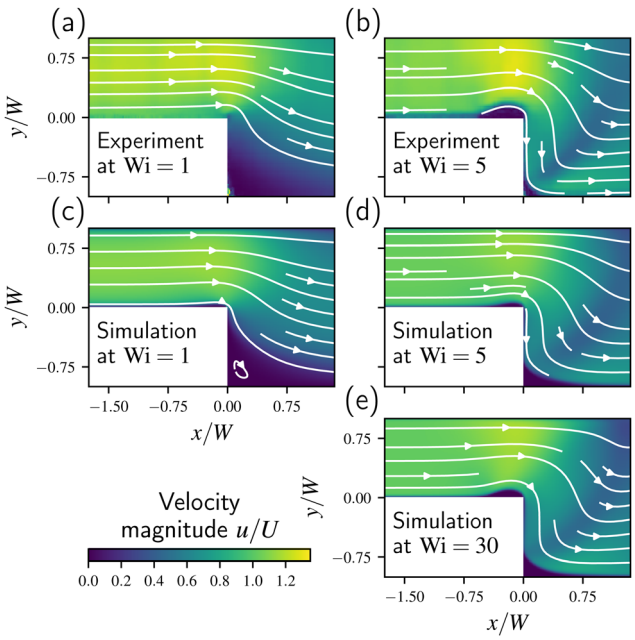

Fig. 4 Velocity magnitude u and streamlines in the expansion phase for the expansion–contraction $D = W$ and $L = 5W$ at Wi = 1 and Wi = 5 obtained from (a) and (b) the time-averaged experimental μ-PIV data and (c)–(e) the steady-state simulation. A better match with the experiment at Wi = 5 is obtained by the steady-state simulation of Wi = 30, see (e). The velocities are normalized using the flow rate and all spatial dimensions are normalized with the channel width W. In (b), (d), and (e), we note the lip vortex at the upstream re-entrant corner and the corner vortex in the downstream salient corner.

Open Access Article. Published on 22 August 2024. Downloaded on 1/20/2026 11:14:46 PM.
This article is licensed under a Creative Commons Attribution 3.0 Unported Licence.

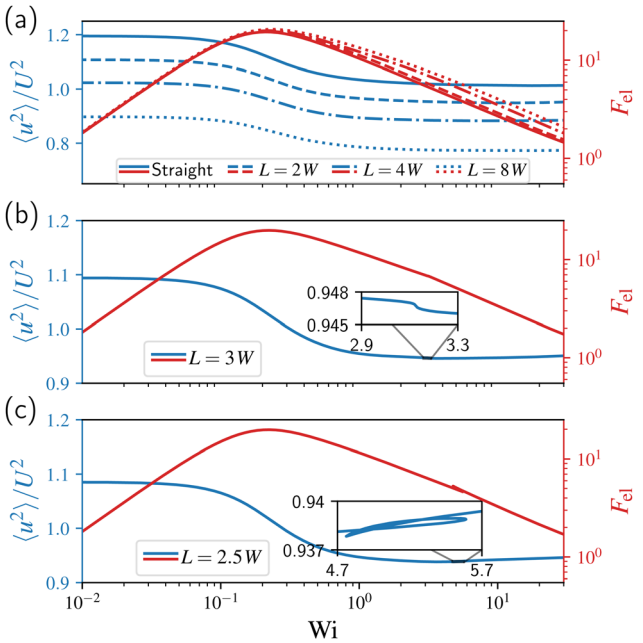

Fig. 5 Mean squared velocity $\langle u^2\rangle/U^2$ and elastic Helmholtz free energy F_{el} compared to Wi for (a) a straight channel with a total length $31W$ as well as concavities of various lengths L, (b) an expansion–contraction with length $L = 3W$ showing a potentially supercritical behavior, and (c) an expansion–contraction with length $L = 2.5W$ showing a subcritical behavior. All concavities have a depth $D = W$.

velocity and Helmholtz free energy to provide a big picture on the fluid behavior in terms of Wi.

3.2 Mean squared velocity and elastic Helmholtz free energy

To provide a general idea about the fluid behavior, we look at the mean squared velocity over the simulation domain Ω and the elastic Helmholtz free energy of the system in relation to Wi. Overall, these results are similar to those of the straight channel, which is shown in Fig. 5(a). The mean squared velocity exhibits a progressive decrease, with a notable inflection point around Wi $\approx$ 0.15. The value reaches its minimum approximately at Wi $\approx$ 17 for the straight channel, before exhibiting a gradual resurgence. However, this minimum is notably variable across different expansion–contraction and cavity configurations. The initial decrease in the mean squared velocity is expected and due to the flattening of the flow profile within the channel, where for the straight channel the theoretical lower limit is $\langle u^2\rangle > U^2$.‡ In contrast, the increase is surprising as it suggests a change, albeit small, in the high shear region near the walls at very large Wi, at least for steady-state flow. This is potentially linked to the end of the shear-banding regime in Fig. 2(a), where the local shear rate at the wall is high and the stress at the wall increases with shear rate beyond the stress plateau.

‡ This limit value corresponds to a completely flat flow profile with slip on the walls. We emphasize that with the no-slip boundary condition the limit cannot be reached.

The elastic Helmholtz free energy linearly increases with Wi until reaching a maximum at Wi $\approx$ 0.21 and then decays as $\sim 1/\sqrt{\mathrm{Wi}}$ over the remaining range of considered Wi values. The maximum appears to coincide with the onset of shear-thinning before any shear bands are expected to form, see Fig. 2(a) and note Wi $\approx \lambda\dot{\gamma}$ for the onset. After the onset of shear-thinning and when the shear localizes, stretching of the micelles is expected to take place only in the regions of high shear rate close to the walls. Meanwhile, the micelles in the plug flow within the bulk, which corresponds to a low shear band, should exhibit minimal, if any stretching.[110–113] As the flow rate increases, the high shear rate regions near the walls become narrower and the elastic Helmholtz free energy decreases, explaining the maximum in the elastic Helmholtz free energy.

The channels with concavities mostly follow the behavior described above for a straight channel. However, in a few cases corresponding to shorter contraction–expansions, deviations from such behaviour are observed. In some cases, for example, we observe a sudden small drop in the mean squared velocity indicating a potentially supercritical behavior, such as shown in the insert to Fig. 5(b). In other cases, we observe multiple values in energy at moderate to large fixed Wi, with an example displayed in Fig. 5(c). While some of these are clear artifacts from the numerical method and mesh, others are qualitatively retained even upon mesh refinement. Nevertheless, as mentioned before, it is not entirely clear if these are numerical artifacts or real. To fully establish this, higher resolution simulations are likely required. We discuss this further in the ESI,† Section S5, specifically for the channel $D = W$ and $L = 2.5W$ shown in Fig. 5(c).

3.3 Flow structures

We now describe the flow structures as we change the length L and depth D from an expansion–contraction ($L > D + W$) to a cavity flow ($L < D + W$). This includes intermediate "transitional" flow regimes that we describe as "short expansion–contractions" ($L \gtrsim D + W$) as well as "long cavities" ($L \lesssim D + W$). The data shown in this section uses the steady state simulation with first order continuation in Wi, with separate simulations for verifying steadiness. As stated previously, we focus on the structure inside the cavity or between the expansion and contraction planes.

3.3.1 Expansion–contraction flows. If L is large compared to D, we observe expansion–contraction flows which consist of separate corner vortices at the salient corners of the expansion and contraction phases. Comparing the flow at two different Weissenberg numbers Wi = 0.1 and Wi = 10, see Fig. 6(a) and (b), respectively, we observe that the corner vortex at the expansion appears to shrink. In contrast, the one at the contraction appears to grow and cover the entire corner. We also note vertical lip vortices not apparent in Fig. 6 which we will discuss shortly.

Before taking a closer look at the corner or lip vortices, however, we first consider the interaction between the expansion and contraction phases. Both Fig. 6(a) and (b) appear to

 This journal is © The Royal Society of Chemistry 2024

Open Access Article. Published on 22 August 2024. Downloaded on 1/20/2026 11:14:46 PM.
This article is licensed under a Creative Commons Attribution 3.0 Unported Licence.

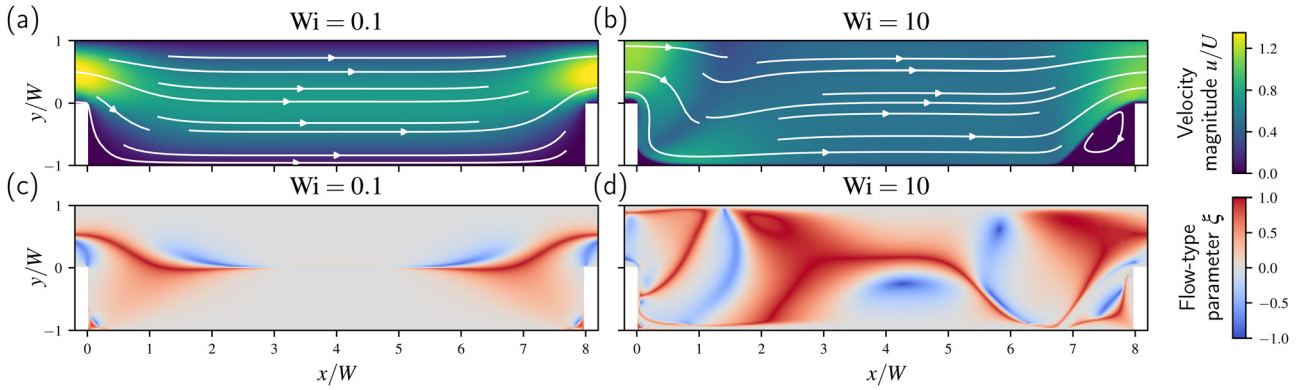

Fig. 6 (a) and (b) Velocity magnitude u with streamlines and (c) and (d) flow-type parameter ξ for the expansion–contraction with depth $D = W$ and length $L = 8W$ at a Weissenberg number (a) and (c) Wi = 0.1 and (b) and (d) Wi = 10. The displayed data is obtained from the steady-state numerical simulations. We note that in (a) the expansion and contraction phases are independent, as shown by (c) the flow-type parameter displaying pure shear flow ($\xi = 0$) between expansion and contraction phases, while in (b) they interact (d) with both rotational ($\xi = -1$) and extensional ($\xi = 1$) flow being present.

consists of properly separated expansion and contraction phases based on the velocity magnitude and streamlines (*i.e.*, the flow appears to become fully-developed in the region between the expansion and contraction planes). However, while this is true for the former, it is not the case for latter. To see this, we use the flow-type parameter ξ,[114–116] § defined as:

$$\xi = \frac{0.5\|\dot{\gamma}\| - \|\mathbf{W}\|}{0.5\|\dot{\gamma}\| + \|\mathbf{W}\|}, \tag{10}$$

where $\dot{\gamma}$ is the deformation rate tensor, $\mathbf{W}$ is the rotation rate tensor, given by the skew-symmetric part of the velocity gradient, and $\|\cdot\|$ denotes the Frobenius norm. The flow-type parameter ξ is useful to distinguish between pure rotational ($\xi = -1$), shear ($\xi = 0$), and extensional ($\xi = 1$) flows. In a straight channel we expect only shear flow, which similarly occurs if the expansion and contraction phases do not interact. This is typically the case at low Wi, shown in Fig. 6(c), while at higher Wi values the expansion and contraction phases interact, see Fig. 6(d). This interaction is also expected to affect the corner vortex sizes.

A closer look at the corner vortices shows that the corner vortex at the expansion decreases in size as the Weissenberg number Wi increases, after a brief span of Wi $\lesssim 1$ where its size changes little for depths $D \geq W$, displayed in Fig. 7(a) and (c). Note that the size here is measured along the length L of the expansion–contraction by extrapolating a zero stream-wise velocity to the wall. At large Wi values the upstream corner vortex starts to slowly grow again. To provoke a better data collapse, though not perfect, Fig. 7(c) uses a different definition of the Weissenberg number: since the corner vortices are inside the concavity, we should expect them to relate to the depth D. We thus define $\mathrm{Wi}_D = \lambda U/D$. This follows in part the results for the 4-1 contraction channel, where the corner vortex is better described when scaled using the upstream height.[8] In contrast to the depth D, the length L should not play a significant role because the expansion and contraction phases separate further as this parameter is increased. With the modified Weissenberg number Wi_D the expansion corner vortex starts to decrease around $\mathrm{Wi}_D \approx 2$ for $D \geq W$, as shown in Fig. 7(c). The breakdown for $D = 0.5W$ is attributed to the stress diffusion with the interface width becoming sizeable in comparison to the other length scales,[99] causing the corner vortex to smear out. Furthermore, the measured vortex size is generally smaller than its largest extent due to a "bulge" structure where streamlines above the vortex curve back near the wall, previously described by Sato *et al.*[34]

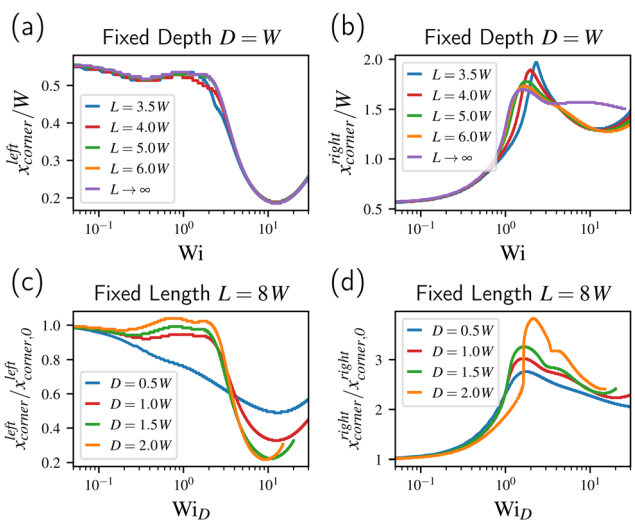

Fig. 7 Corner vortex sizes measured along the concavity length for (a) the left corner at fixed depth $D = W$, (b) the right corner at fixed depth $D = W$, (c) the left corner normalized with the Newtonian size at fixed length $L = 8W$, and (d) the right corner normalized with the Newtonian size at fixed length $L = 8W$. The data shown is based on the steady-state numerical simulations. The Weissenberg number Wi_D uses the depth D as characteristic length in place of to the channel width W in eqn (1). Note that for (a) and (b) Wi_D = Wi.

§ Patils *et al.*[114] use the symbol ψ instead. Giesekus[115] defines $\rho = 2\sqrt{-I_2(\mathbf{W})/I_2(\dot{\gamma})}$ using the second invariant I_2, where the flow-type parameter is recovered as $\xi = (1 - \rho)/(1 + \rho)$.

Open Access Article. Published on 22 August 2024. Downloaded on 1/20/2026 11:14:46 PM.
This article is licensed under a Creative Commons Attribution 3.0 Unported Licence.

The size of the corner vortex at the contraction phase sharply increases with increasing Wi (or Wi_D), see Fig. 7(b) and (d), before shrinking after attaining a maximum and then, together with the other corner vortex, growing yet again but at a slower rate. The maximum occurs at around $\mathrm{Wi}_D \approx 2$, similar to the decrease in the expansion corner vortex. The initial increase followed by a decrease has been previously reported by Hooshyar and Germann[73] in the 4-1 contraction channel for a shear-banding fluid, who attributed the increase to shear-thinning and the decrease to shear-banding. The eventual increase of the corner vortex, however, appears to relate to an interaction with the expansion phase, as we observe instead a saturation and further decrease in size with a solitary contraction. This is in contrast to the growth of the corner vortex at the expansion, which is also exhibited even without a contraction phase.

We further remark on lip vortices attached to the vertical walls at the re-entrant corners of the expansion–contraction geometries, as shown in Fig. 8, where we emphasize the expanded scaling of the x-axis due to the extreme narrowness of the vortices in the x-direction. In some cases (as in Fig. 8) such vertical lip vortices were observed at both the expansion and contraction planes, and in other cases at the expansion plane only. However, such a lip vortex at only the contraction plane was never observed. This may be explained by the relatively large size of the corner vortex at the contraction plane which engulfs any lip vortices that potentially form. Indeed, with increasing Wi, a lip vortex fixed at the contraction plane (*e.g.*, Fig. 8(b)) is consumed by the growing corner vortex, thus forming a single vortex covering the entire corner such as in Fig. 6(b). For non-shear-thinning fluids, numerical studies typically predict the opposite and this lip vortex grows while the corner vortex decreases in size.[9,10,23] The corner vortex at the expansion plane shrinks with increasing Wi and the re-entrant corner is expected to promote the formation of at least one lip vortex. This is in relation to the Pakdel–McKinley criterion,[31,117] which predicts elastic instabilities due to strong curvature of streamlines and high first normal stress difference along them. The lip vortex decreases the curvature and typically forms upstream, discussed in the ESI,† Section S4, rather than downstream of the expansion re-entrant corner. A similar observation was reported by Wojcik *et al.*[118] for a sharp bend where non-Newtonian flows typically form a lip vortex upstream, corresponding to "elasticity driven" lip vortices. Similar lip vortices have been reported by Poole *et al.*[2,3] for expansion flows, who proposed their explanation *via* the Pakdel–McKinley criterion. The vertical lip vortex at the expansion plane detaches from the re-entrant corner with increasing Wi and moves to merge with the corner vortex. We emphasize that these vertical lip vortices only appear if the depth D is large enough compared to the channel width W. This is in line with numerical work on contraction channels by Alves *et al.*[8] for a shear-thinning fluid.

Finally, we also point out that the expansion–contraction flows exhibit ternary vortices, Moffatt-like vortices[119] that we will describe in more detail for cavity flows, and that the flows further show time dependence starting around $\mathrm{Wi} \gtrsim 4$. Time-dependence is, however, only observed if the depth $D \geq 1.5W$. We recall that time dependence is generally inadequately captured by the Giesekus model[82] which may offer an explanation for this rather restricted observation on time-dependent flows.

3.3.2 Transitional regime: short expansion–contractions and long cavities. As we decrease L with respect to D we reach "short expansion–contractions" which at low Wi resemble expansion–contraction flows but deviate as Wi increases. In particular, these flows frequently display corner vortices that are connected, but with a bridge small enough to differentiate it from a single recirculation unequivocally characterizing cavity flows. One example of this is shown in Fig. 9(a), where we further observe that the shear localization occurs at some distance from the boundaries of the vortices. However, for

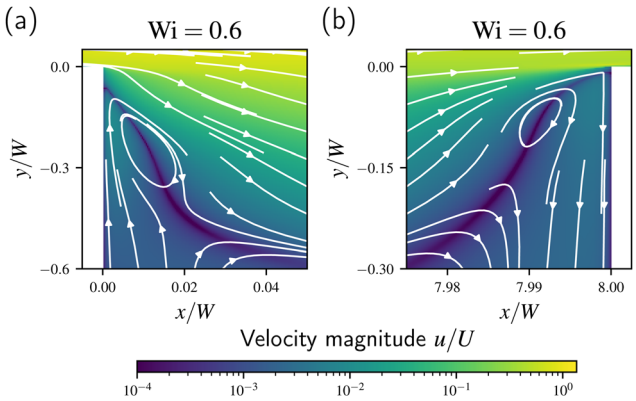

Fig. 8 Velocity magnitude u (using a $\log_{10}$-scale) and streamlines for the expansion–contraction with $D = W$ and $L = 8W$ at Wi = 0.5 focused on (a) the vertical lip vortex at the wall of the expansion phase and (b) the vertical lip vortex at the wall of the contraction phase. These lip vortices are narrow and we emphasize the different scaling in x- and y-axis.

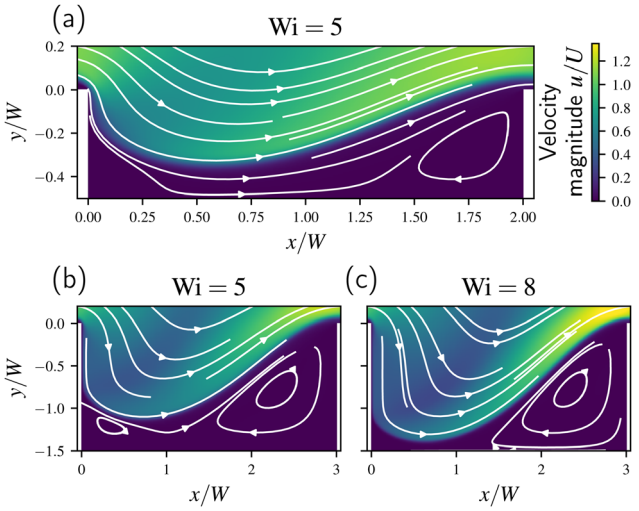

Fig. 9 Velocity magnitude u and streamlines for the short expansion–contractions using the steady-state numerical data with (a) depth $D = 0.5W$ and length $L = 2W$; (b) and (c) depth $D = 1.5W$ and length $L = 3W$ at two different Weissenberg numbers. We note the shear localization in (a) which does not align with the the boundaries of the vortices, and the extra recirculation inside the concavity in (b) compared to (c).

Open Access Article. Published on 22 August 2024. Downloaded on 1/20/2026 11:14:46 PM.
This article is licensed under a Creative Commons Attribution 3.0 Unported Licence.

larger depths, a single recirculation zone spanning the length of the concavity is observed, such as in Fig. 9(b), where in this case the shear localization coincides with the boundaries of the vortices. This single large recirculation zone typical of "cavity" flow splits again into two separated corner vortices at higher Wi, see Fig. 9(c), now appearing similar to an expansion–contraction flow.

The transitional regime proves to be numerically challenging. Alongside the deeper expansion–contraction flows, it is in particular for the short expansion–contraction at higher Wi that the pseudo-arclength continuation is required but, as mentioned before, likely does not yield accurate results. This may be due to a frustrated energy landscape, which makes the constrained minimization problem underlying the finite element method difficult to solve. It may, however, also be due to the mesh resolution and shear localization in the bulk where the elements are larger compared to the walls and the top of the concavity. These numerical issues are again discussed in the ESI,† Section S5, where we focus specifically on the short expansion–contraction.

Decreasing the concavity length further leads to what we term a "long cavity", illustrated in Fig. 10 where we only focus on the cavity section. Similar to the short expansion–contraction, the long cavity behaves as an expansion–contraction for low Wi values, Fig. 10(a), but for higher Wi transitions to a cavity with a single recirculation zone containing two vortices side-by-side, such as in Fig. 10(b). Upon further increasing Wi a single vortex forms, see Fig. 10(c). In the short expansion–contraction the distance of the shear localization from the bottom wall of the concavity decreases as Wi increases and thus expansion–contraction flow re-appears at high Wi. In contrast, for the long cavity the shear localization continuously recedes from the wall as Wi increases and the flow structures remain resembling those expected of cavity flow. Finally, as shown in Fig. 10(d) for even higher Wi the vortex splits again into two as the shear localization creates a sizeable cavity.

We expect both the short expansion–contraction and the long cavity to be affected by the shear localization, such as from shear-thinning or shear-banding. For example, as we have seen in the prior section and as argued by Hooshyar and Germann[73] for the 4-1 contraction, the decrease in the corner vortex at the contraction plane is related to shear-banding. This likely has an effect on the short expansion–contraction and the absence of such a decrease may prevent the short expansion–contraction from recovering an expansion–contraction flow. On the other hand, for a fluid that is neither shear-thinning nor shear-banding it is often observed that this corner vortex decreases in size[9,10,23] which in turn may prevent a long cavity from forming. However, further investigations using different constitutive models are required in order to make a definite statement.

3.3.3 Cavity flows. Cavity flows arise as $L \lesssim D$ and are differentiated based on their depth D. Within the considered geometries, we observe single, two, three, four, or five vortices vertically stacked with more vortices appearing as D increases. We remark that at small Wi the bottom vortex is often split into two horizontal vortices within a single encapsulating recirculation zone spanning the length L. Here, the bottom vortex is only a fraction of the height compared to the vortices above and reminiscent of a long cavity, illustrated by Fig. 11(a). With increasing Wi values, this

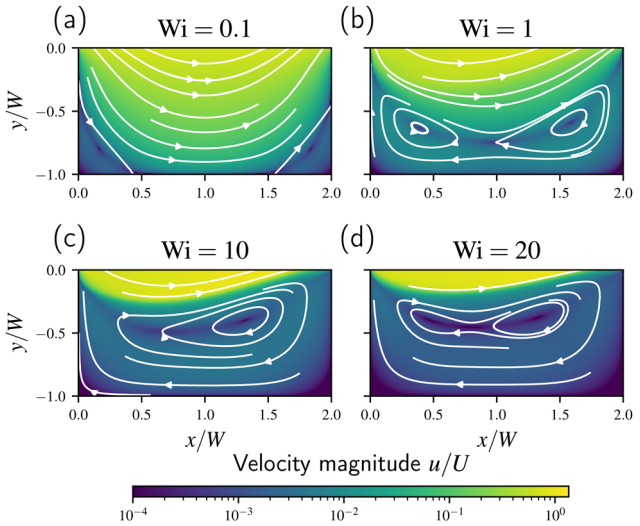

Fig. 10 Velocity magnitude u (using a $\log_{10}$-scale) and streamlines for a long cavity, where $D = W$ and $L = 2W$, using the steady-state numerical data at (a) Wi = 0.1, (b) Wi = 1, (c) Wi = 10, and (d) Wi = 20. We note the the change from (a) an expansion–contraction towards (c) and (d) a cavity with different number of vortices.

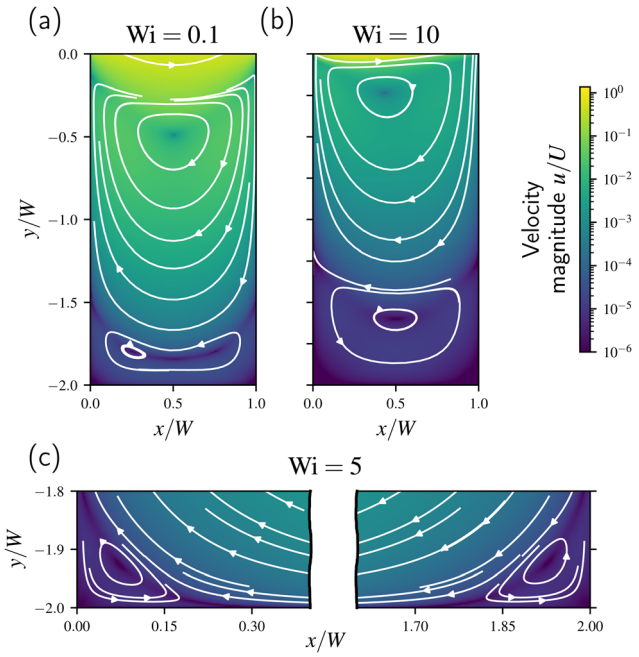

Fig. 11 Steady-state velocity magnitude u (using $\log_{10}$-scale) and streamlines for the cavities (a) and (b) with length $L = W$ and depth $D = 2W$ or (c) with length $L = 2W$ and depth $D = 2W$, at different Wi. We note the two vortices at the bottom in (a) compared to the single vortex in (b). Furthermore, the cavity and channel are separated by a region of localized shear reminiscent of a lid-driven cavity, specifically as Wi is increased. For the square cavity (c) we note the ternary vortex structures that form at the salient corners of the cavity.

Open Access Article. Published on 22 August 2024. Downloaded on 1/20/2026 11:14:46 PM.
This article is licensed under a Creative Commons Attribution 3.0 Unported Licence.

recirculation at the bottom grows in height and a single vortex forms, such as in Fig. 11(b).

Overall, the cavity flow appears to approach a lid-driven cavity flow with increasing Wi, with the primary flow barely penetrating into the cavity. In this context, we can connect our observations to prior studies for lid-driven cavities. For example, given the low local Wi within the cavity due to the slow flow, we connect the split vortices at the bottom to the Newtonian case: they arise and merge from vortices located at the bottom corners as the depth D increases,[24,29] see Fig. 11(c). These are again the Moffatt vortices[119] mentioned in prior sections. Furthermore, as the Wi value increases the shear localization at the top of the cavity moves upwards resulting in a larger effective depth D and better approximation to the lid-driven cavity that also allows the corner vortices to merge, as shown in Fig. 11(a) and (b). The same process permits a change in the number of vortices, for example from a single vortex to two vortices stacked with the bottom split that occurs for the channel $D = 2.5W$ and $L = 1.5W$ (see also Fig. S9 in the ESI†). With respect to viscoelastic lid-driven flows, we emphasize the upstream shift of the upper vortex center from Fig. 11(a) and (b), which is due to the generation of large normal stresses as viscoelasticity increases.[33]

The analogy to the lid-driven cavity is not perfect but can be verified by fixing the aspect ratio D/L for different lengths L. This is shown in Fig. 12 for $D/L = 2$, where we use the flow-type parameter ξ introduced in Section 3.3.1 to show details masked by the direct velocity field. We have corrected the Weissenberg number by the geometric factor W/L, yielding what is considered a Deborah number $De = \lambda U/L$ for the lid-driven cavity.[32,59] This is to account for the different velocities when scaling the channel dimensions. In particular, the scaling ensures that a fluid particle in the primary flow above the cavity, which drives the flow inside, takes an equal amount of time to travel the cavity length L. We highlight the clear differences in Fig. 12(a) and (d) compared to the latter two pairs. This presumably relates to the stress diffusion and the interface width,[99] similar to the corner vortex at the expansion phase discussed for expansion–contraction flows. This in turn changes the shape of the driving velocity, or regularization,[33] for the lid-driven cavity. Therefore, we cannot completely decouple the flow inside the cavity from the main channel when D or L are small.

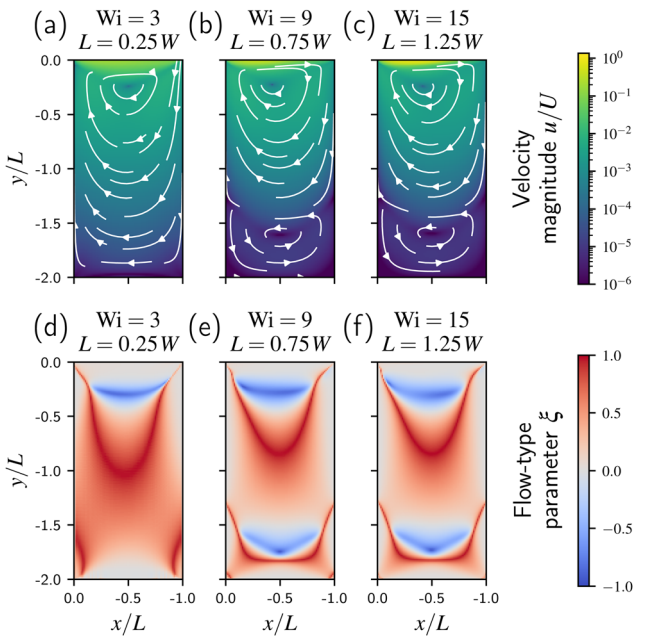

Fig. 12 Cavities of fixed ratio $D/L = 2$. Displayed are (a)–(c) the steady-state velocity (using a $\log_{10}$-scale) with streamlines and (d)–(f) the flow-type parameter ξ. The length varies from (a) and (d) $L = 0.25W$, to (b) and (e) $L = 0.75W$, and finally (c) and (f) $L = 1.25W$. We adjust the Weissenberg numbers such that the Deborah number $De = Wi \cdot W/L = 12$ remains constant.

3.4 Flow summary: phase diagrams

We summarize the observations of the prior sections as phase diagrams in L–D at different Wi in Fig. 13, alongside some representative examples of corresponding flow states. We use again the first order continuation with the steady-state simulation. However, we have supplemented the data with simulations using the pseudo-arclength continuation where the first order continuation fails. These are marked using an overlay with diagonal lines at a 135° angle. Additionally, we indicate the onset of time-dependence (diagonal lines at a 45° angle) based on separate unsteady simulations. Several flow structures are differentiated, ranging from different types of deep cavities to expansion–contraction flows. A complete classification can be found in the ESI,† Section S6.

Overall, we differentiate two clearly distinct categories: cavity flows (blue shadings), characterized by recirculation zones spanning the length L, and expansion–contraction flows (red shading), characterized by separate corner vortices in the salient corners. These are separated by a more ambiguous transitional regime (white shading), which exhibits characteristics of both. Generally, we find that expansion–contraction flows occur when the length L exceeds the sum of the depth D and channel width W, *i.e.*, $L > D + W$. On the other hand, the flow is typically a cavity flow for $L \lesssim D + W$. This includes long cavities, which contain two vortices side-by-side within a single encapsulating recirculation zone. We emphasize that the exact flow structures in terms of number of vortices or their size depend on the Wi value. We further emphasize that the transition applies to the lengths L and depths D considered within this study. This will clearly break down as D or L are further decreased. In fact, this is already apparent in our discussion on the corner vortex sizes in the expansion–contraction flows, see Fig. 7(c), and in the discussion on the applicability of the lid-driven cavity analogy for the cavity, see Fig. 12. In both cases, we attribute these deviations to the interface width that becomes significant in size compared to the other (geometric) length scales and thus cannot be ignored. On the other hand, we also expect a breakdown simply based on geometric consideration. For example, a very shallow ($D \ll W$) channel but with a comparable length and channel width $L \approx W$ is unlikely to sustain a cavity flow even if $L < D + W$. Nevertheless, the

 This journal is © The Royal Society of Chemistry 2024

Open Access Article. Published on 22 August 2024. Downloaded on 1/20/2026 11:14:46 PM.
This article is licensed under a Creative Commons Attribution 3.0 Unported Licence.

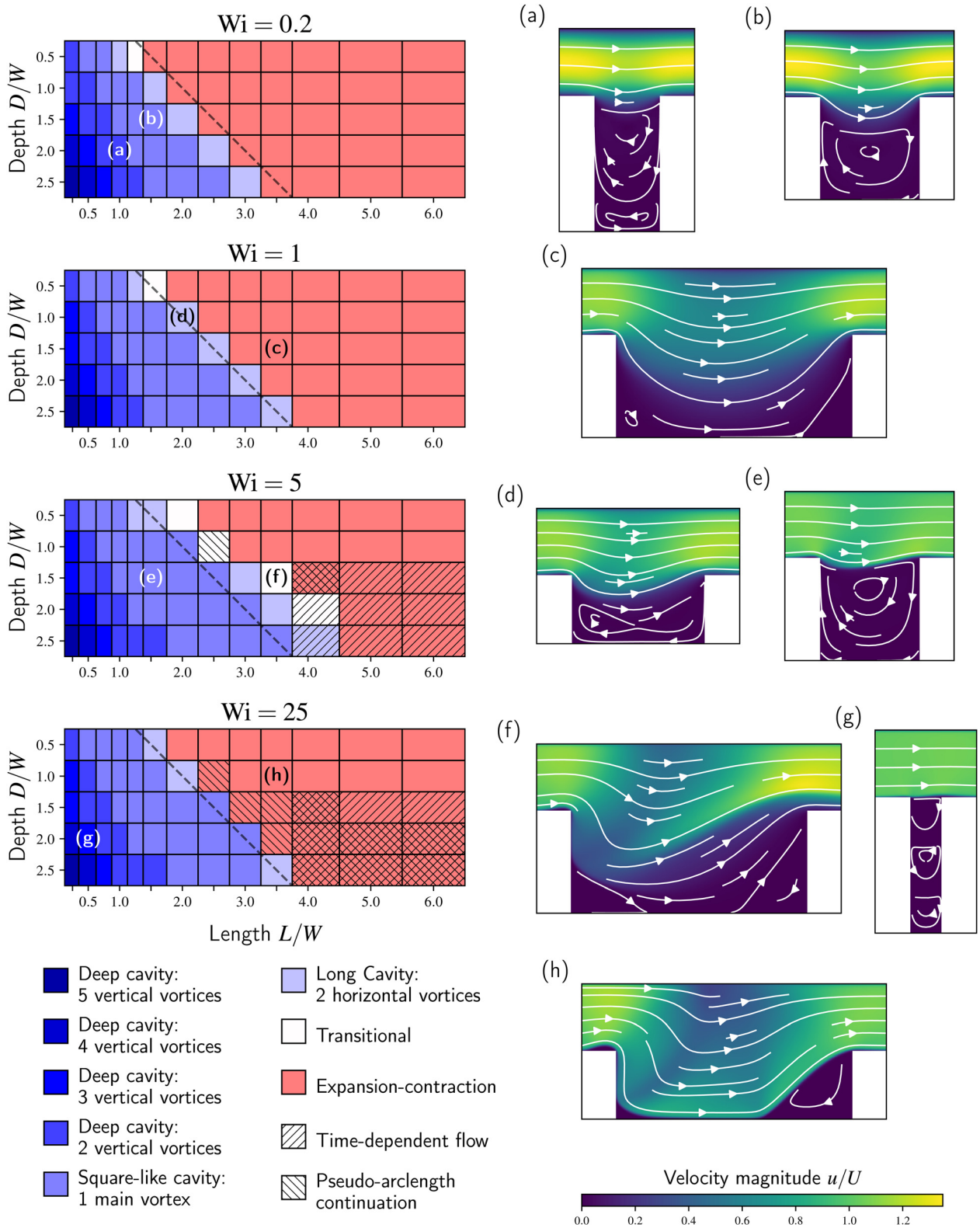

Fig. 13 Different flows observed based on depth D and length L at Wi = 0.2, Wi = 1, Wi = 5, and Wi = 25 using the simulation data. The different color indicate the different flow structures, ignoring finer details such as additional lip vortices in expansion–contractions. We highlight (a) and (g) deep cavities, (b) and (e) square cavities, (d) a long cavity, (f) a short expansion–contraction, and (c) and (h) expansion–contractions. The dashed line indicates the transition $L = D + W$. We further mark the cases where time-dependence was observed (45°-diagonals) and where the pseudo-arclength continuation was required (135°-diagonals).

Open Access Article. Published on 22 August 2024. Downloaded on 1/20/2026 11:14:46 PM.
This article is licensed under a Creative Commons Attribution 3.0 Unported Licence.

inclusion of the channel width W in the classification appears useful in the geometries we have considered and allows the inclusion of long cavities while excluding short expansion–contractions.

4 Conclusions

In this study, we have investigated the creeping flow of a fluid that exhibits strong shear localization through a geometry with a concavity on one wall. We employ two-dimensional numerical simulations, which were validated against experimental measurements of the flow at the expansion phase of the concavity. By changing the depth D and length L, different flow regimes were identified: cavity flow ($L \lesssim D + W$), expansion–contraction flow ($L > D + W$), and a complex transitional regime separating the former two. Our work connects to many prior studies, which typically focus on a single aspect of our geometry or use non-shear-banding fluids. However, the concavities investigated in our study are not symmetric about the channel centreline, as is typically the case for studies on expansions and/or contractions. We also note a lip vortex upstream of the cavity or expansion plane at the re-entrant corner, which was similarly found in other studies[2,3] and whose discussion can be found in the ESI,† Section S4. We simply note here that this lip vortex qualitatively differs in behavior from the structures inside the concavity, specifically in the limit of large depths D and lengths L. In this limit, the lip vortex appears to be independent of the ratio D/L and the flow inside the concavity. In contrast, the flow structures inside are expected to entirely depend on the ratio D/L.

While we have examined different depths and lengths for the concavity, future studies looking at concavities at greater depths would be beneficial to validate the trends we have identified. Currently, we are limited by the computational cost associated with the large meshes required by their geometries, but the use of adaptive meshes or different programming methodologies to extend parallelization can potentially overcome this issue. The Giesekus constitutive model also provides no insights into the breaking and reformation that wormlike micelles exhibit. The use of a constitutive model including these effects, such as Vasquez–Cook–McKinley model,[81] would provide additional information on the microstructural behavior of WLM solutions. Furthermore, we have focused on shear-banding fluids but fluids with other rheological properties could also yield important insights.

Finally, while numerical simulations provide an efficient method to explore various geometries and flow conditions, experimental investigations should not be neglected. Specifically conducting thorough experimental analyses in the transitional regime would greatly enhance our understanding and offer valuable insights for future research.

Author contributions

F. H.: conceptualization, data curation, formal analysis, investigation, methodology, software (minor), visualization, writing – original draft; S. V.: methodology (sim.), software, resources (sim.), supervision (sim.), writing – review & editing; C. C. H.: conceptualization (exp.), investigation (exp.), methodology (exp.), resources (exp.), supervision (exp.), writing – review & editing; S. J. H.: conceptualization (exp.), writing – review & editing; A. Q. S.: conceptualization (exp.), resources, writing – review & editing.

Data availability

The data supporting this article are available within the article and the ESI.†

Conflicts of interest

There are no conflicts to declare.

Acknowledgements

We gratefully acknowledge the support of the Okinawa Institute of Science and Technology Graduate University (OIST) and the Scientific Computing and Data Analysis (SCDA) section of the Core Facilities at OIST. The latter provided the supercomputer Deigo, which has been used to process the experimental data and run the simulations. A. Q. S. and S. J. H. gratefully acknowledge funding support from the Japan Society for the Promotion of Science (JSPS, Grant No. 24K00810 and 24K07332, respectively). F. H. thanks Kazumi Toda-Peters for helping design and create the channels and Dr Daniel W. Carlson and Dr Ricardo Arturo López de la Cruz for insightful discussions. Finally, all authors like to extend their gratitude to the referees for their insightful comments and recommendations that have helped improve this manuscript.

References

1 F. T. Pinho, P. J. Oliveira and J. P. Miranda, *Int. J. Heat Fluid Flow*, 2003, **24**, 747–761.
2 R. J. Poole, M. A. Alves, P. J. Oliveira and F. T. Pinho, *J. Non-Newtonian Fluid Mech.*, 2007, **146**, 79–91.
3 R. J. Poole, F. T. Pinho, M. A. Alves and P. J. Oliveira, *J. Non-Newtonian Fluid Mech.*, 2009, **163**, 35–44.
4 K. Chiba, S. Tanaka and K. Nakamura, *J. Non-Newtonian Fluid Mech.*, 1992, **42**, 315–322.
5 B. Yesilata, A. Öztekin and S. Neti, *J. Non-Newtonian Fluid Mech.*, 1999, **85**, 35–62.
6 F. Olsson, *J. Non-Newtonian Fluid Mech.*, 1994, **51**, 309–340.
7 A. Baloch, P. Townsend and M. F. Webster, *J. Non-Newtonian Fluid Mech.*, 1996, **65**, 133–149.
8 M. A. Alves, P. J. Oliveira and F. T. Pinho, *J. Non-Newtonian Fluid Mech.*, 2004, **122**, 117–130.
9 F. Pimenta and M. Alves, *J. Non-Newtonian Fluid Mech.*, 2017, **239**, 85–104.
10 M. Niethammer, H. Marschall and D. Bothe, *Chem. Ing. Tech.*, 2019, **91**, 522–528.

 This journal is © The Royal Society of Chemistry 2024

Open Access Article. Published on 22 August 2024. Downloaded on 1/20/2026 11:14:46 PM.
This article is licensed under a Creative Commons Attribution 3.0 Unported Licence.

11 J. P. Rothstein and G. H. McKinley, *J. Non-Newtonian Fluid Mech.*, 1999, **86**, 61–88.
12 J. P. Rothstein and G. H. McKinley, *J. Non-Newtonian Fluid Mech.*, 2001, **98**, 33–63.
13 L. E. Rodd, T. P. Scott, D. V. Boger, J. J. Cooper-White and G. H. McKinley, *J. Non-Newtonian Fluid Mech.*, 2005, **129**, 1–22.
14 F. Khalkhal and S. Muller, *Phys. Rev. Fluids*, 2022, **7**, 023303.
15 P. P. Jagdale, D. Li, X. Shao, J. B. Bostwick and X. Xuan, *Micromachines*, 2020, **11**, 278.
16 M. K. Raihan, S. Wu, Y. Song and X. Xuan, *Soft Matter*, 2021, **17**, 9198–9209.
17 T. Cochrane, K. Walters, M. F. Webster and W. J. G. Beynon, *Philos. Trans. R. Soc. London, Ser. A*, 1981, **301**, 163–181.
18 J.-H. Kim, A. Öztekin and S. Neti, *J. Non-Newtonian Fluid Mech.*, 2000, **90**, 261–281.
19 M. K. Raihan, P. P. Jagdale, S. Wu, X. Shao, J. B. Bostwick, X. Pan and X. Xuan, *Micromachines*, 2021, **12**, 836.
20 C.-D. Xue, Z.-Y. Zheng, G.-S. Zheng, D.-W. Zhao and K.-R. Qin, *Soft Matter*, 2022, **18**, 3867–3877.
21 X.-Y. Xu, Z.-Y. Zheng, K. Tian, D. Wang, K.-R. Qin and C.-D. Xue, *Phys. Fluids*, 2024, **36**, 042001.
22 G. Yin, Y. Nakamura, H. Suzuki, F. Lequeux and R. Hidema, *Phys. Fluids*, 2024, **36**, 043114.
23 M. Alves, P. Oliveira and F. Pinho, *Annu. Rev. Fluid Mech.*, 2021, **53**, 509–541.
24 P. N. Shankar, *J. Fluid Mech.*, 1993, **250**, 371–383.
25 R. Fattal and R. Kupferman, *J. Non-Newtonian Fluid Mech.*, 2004, **123**, 281–285.
26 R. Fattal and R. Kupferman, *J. Non-Newtonian Fluid Mech.*, 2005, **126**, 23–37.
27 S. Varchanis, A. Syrakos, Y. Dimakopoulos and J. Tsamopoulos, *J. Non-Newtonian Fluid Mech.*, 2019, **267**, 78–97.
28 U. Ghia, K. N. Ghia and C. T. Shin, *J. Comput. Phys.*, 1982, **48**, 387–411.
29 P. N. Shankar and M. D. Deshpande, *Annu. Rev. Fluid Mech.*, 2000, **32**, 93–136.
30 H. C. Kuhlmann and F. Romanò, in *The Lid-Driven Cavity*, ed. A. Gelfgat, Springer International Publishing, Cham, 2019, pp. 233–309.
31 P. Pakdel and G. H. McKinley, *Phys. Rev. Lett.*, 1996, **77**, 2459–2462.
32 P. Pakdel, S. H. Spiegelberg and G. H. McKinley, *Phys. Fluids*, 1997, **9**, 3123–3140.
33 R. Sousa, R. Poole, A. Afonso, F. Pinho, P. Oliveira, A. Morozov and M. Alves, *J. Non-Newtonian Fluid Mech.*, 2016, **234**, 129–138.
34 H. Sato, M. Kawata, R. Hidema and H. Suzuki, *J. Non-Newtonian Fluid Mech.*, 2022, **310**, 104946.
35 M. Pavlidis, G. Karapetsas, Y. Dimakopoulos and J. Tsamopoulos, *J. Non-Newtonian Fluid Mech.*, 2016, **234**, 201–214.
36 A. Marousis, D. Pettas, G. Karapetsas, Y. Dimakopoulos and J. Tsamopoulos, *J. Fluid Mech.*, 2021, **915**, A98.
37 M. E. Cates, *Macromolecules*, 1987, **20**, 2289–2296.
38 J. D. Peterson and M. E. Cates, *J. Rheol.*, 2020, **64**, 1465–1496.
39 J. D. Peterson and M. E. Cates, *J. Rheol.*, 2021, **65**, 633–662.
40 J. D. Peterson and L. Gary Leal, *J. Rheol.*, 2021, **65**, 959–982.
41 J. P. Rothstein, *Rheol. Rev.*, 2008, **2008**, 1–46.
42 J. P. Rothstein and H. Mohammadigoushki, *J. Non-Newtonian Fluid Mech.*, 2020, **285**, 104382.
43 A. Sambasivam, A. V. Sangwai and R. Sureshkumar, *Phys. Rev. Lett.*, 2015, **114**, 158302.
44 S. Dhakal and R. Sureshkumar, *ACS Macro Lett.*, 2016, **5**, 108–111.
45 R. Omidvar, A. Dalili, A. Mir and H. Mohammadigoushki, *J. Non-Newtonian Fluid Mech.*, 2018, **252**, 48–56.
46 A. A. Dey, Y. Modarres-Sadeghi and J. P. Rothstein, *Phys. Rev. Fluids*, 2018, **3**, 063301.
47 C. C. Hopkins, S. J. Haward and A. Q. Shen, *Small*, 2020, **16**, 1903872.
48 A. A. Dey, Y. Modarres-Sadeghi, A. Lindner and J. P. Rothstein, *Soft Matter*, 2020, **16**, 1227–1235.
49 A. A. Dey, Y. Modarres-Sadeghi and J. P. Rothstein, *J. Fluids Struct.*, 2020, **96**, 103025.
50 P. Nghe, S. M. Fielding, P. Tabeling and A. Ajdari, *Phys. Rev. Lett.*, 2010, **104**, 248303.
51 S. J. Haward, F. J. Galindo-Rosales, P. Ballesta and M. A. Alves, *Appl. Phys. Lett.*, 2014, **104**, 124101.
52 P. F. Salipante, C. A. E. Little and S. D. Hudson, *Phys. Rev. Fluids*, 2017, **2**, 033302.
53 J. Yang, *Curr. Opin. Colloid Interface Sci.*, 2002, **7**, 276–281.
54 S. Ezrahi, E. Tuval and A. Aserin, *Adv. Colloid Interface Sci.*, 2006, **128–130**, 77–102.
55 C. A. Dreiss, *Soft Matter*, 2007, **3**, 956–970.
56 S. Honarmand, M. Mehraei, Z. A. Radmoghadam, E. Mohammadi, M. Dastjerdi, S. Akbari and A. Akbari, *Nanosci. Technol.*, 2023, **10**, 1–32.
57 T. Divoux, M. A. Fardin, S. Manneville and S. Lerouge, *Annu. Rev. Fluid Mech.*, 2016, **48**, 81–103.
58 S. Lerouge and P. D. Olmsted, *Front. Phys.*, 2020, **7**, 246.
59 R. J. Poole, *Rheol. Bull.*, 2012, **53**, 32–39.
60 J. L. White, *J. Appl. Polym. Sci.*, 1964, **8**, 2339–2357.
61 Y. Zhao, P. Cheung and A. Q. Shen, *Adv. Colloid Interface Sci.*, 2014, **211**, 34–46.
62 J. A. Pathak and S. D. Hudson, *Macromolecules*, 2006, **39**, 8782–8792.
63 S. J. Haward, T. J. Ober, M. S. Oliveira, M. A. Alves and G. H. McKinley, *Soft Matter*, 2012, **8**, 536–555.
64 N. Dubash, P. Cheung and A. Q. Shen, *Soft Matter*, 2012, **8**, 5847–5856.
65 M. Y. Hwang, H. Mohammadigoushki and S. J. Muller, *Phys. Rev. Fluids*, 2017, **2**, 043303.
66 Y. Zhang, H. Mohammadigoushki, M. Y. Hwang and S. J. Muller, *Phys. Rev. Fluids*, 2018, **3**, 093301.
67 T. Hashimoto, K. Kido, S. Kaki, T. Yamamoto and N. Mori, *Rheol. Acta*, 2006, **45**, 841–852.
68 V. Lutz-Bueno, J. Kohlbrecher and P. Fischer, *J. Non-Newtonian Fluid Mech.*, 2015, **215**, 8–18.

Open Access Article. Published on 22 August 2024. Downloaded on 1/20/2026 11:14:46 PM.
This article is licensed under a Creative Commons Attribution 3.0 Unported Licence.

69 R. M. Matos, M. A. Alves and F. T. Pinho, *Exp. Fluids*, 2019, **60**, 145.
70 E. Jafari Nodoushan, Y. J. Lee, G.-H. Lee and N. Kim, *Phys. Fluids*, 2021, **33**, 093112.
71 J. López-Aguilar, M. Webster, H. Tamaddon-Jahromi and O. Manero, *J. Non-Newtonian Fluid Mech.*, 2014, **204**, 7–21.
72 H. Tamaddon Jahromi, M. Webster, J. Aguayo and O. Manero, *J. Non-Newtonian Fluid Mech.*, 2011, **166**, 102–117.
73 S. Hooshyar and N. Germann, *Polymers*, 2019, **11**, 417.
74 M. R. Stukan, E. S. Boek, J. T. Padding, W. J. Briels and J. P. Crawshaw, *Soft Matter*, 2008, **4**, 870–879.
75 M. R. Stukan, E. S. Boek, J. T. Padding and J. P. Crawshaw, *Eur. Phys. J. E: Soft Matter Biol. Phys.*, 2008, **26**, 63–71.
76 C. Sasmal, *Phys. Fluids*, 2020, **32**, 013103.
77 R. Larson and P. S. Desai, *Annu. Rev. Fluid Mech.*, 2015, **47**, 47–65.
78 S. Varchanis, S. J. Haward, C. C. Hopkins, J. Tsamopoulos and A. Q. Shen, *J. Non-Newtonian Fluid Mech.*, 2022, **307**, 104855.
79 H. Giesekus, *J. Non-Newtonian Fluid Mech.*, 1982, **11**, 69–109.
80 M. Johnson and D. Segalman, *J. Non-Newtonian Fluid Mech.*, 1977, **2**, 255–270.
81 P. A. Vasquez, G. H. McKinley and L. Pamela Cook, *J. Non-Newtonian Fluid Mech.*, 2007, **144**, 122–139.
82 R. L. Moorcroft and S. M. Fielding, *J. Rheol.*, 2014, **58**, 103–147.
83 H. Rehage and H. Hoffmann, *J. Phys. Chem.*, 1988, **92**, 4712–4719.
84 H. Rehage and H. Hoffmann, *Mol. Phys.*, 1991, **74**, 933–973.
85 C. C. Hopkins, S. J. Haward and A. Q. Shen, *Soft Matter*, 2022, **18**, 4868–4880.
86 N. Burshtein, S. T. Chan, K. Toda-Peters, A. Q. Shen and S. J. Haward, *Curr. Opin. Colloid Interface Sci.*, 2019, **43**, 1–14.
87 A. Liberzon, T. Käufer, A. Bauer, P. Vennemann and E. Zimmer, *OpenPIV/openpiv-python: OpenPIV-Python v0.23.4*, Zenodo, 2021, DOI: 10.5281/zenodo.4409178.
88 A. W. El-Kareh and L. Gary Leal, *J. Non-Newtonian Fluid Mech.*, 1989, **33**, 257–287.
89 C.-Y. D. Lu, P. D. Olmsted and R. C. Ball, *Phys. Rev. Lett.*, 2000, **84**, 642–645.
90 J. H. Snoeijer, A. Pandey, M. A. Herrada and J. Eggers, *Proc. R. Soc. A*, 2020, **476**, 20200419.
91 A. N. Beris and B. J. Edwards, *Thermodynamics of Flowing Systems: with Internal Microstructure*, Oxford University Press, 1994.
92 W. Kuhn, *Kolloid-Z.*, 1934, **68**, 2–15.
93 G. Sarti and G. Marrucci, *Chem. Eng. Sci.*, 1973, **28**, 1053–1059.
94 S. M. Fielding and P. D. Olmsted, *Eur. Phys. J. E: Soft Matter Biol. Phys.*, 2003, **11**, 65–83.
95 O. Radulescu, P. D. Olmsted, J. P. Decruppe, S. Lerouge, J.-F. Berret and G. Porte, *Europhys. Lett.*, 2003, **62**, 230.
96 P. Ballesta, M. P. Lettinga and S. Manneville, *J. Rheol.*, 2007, **51**, 1047–1072.
97 C. Masselon, J.-B. Salmon and A. Colin, *Phys. Rev. Lett.*, 2008, **100**, 038301.
98 M. E. Helgeson, P. A. Vasquez, E. W. Kaler and N. J. Wagner, *J. Rheol.*, 2009, **53**, 727–756.
99 C. Masselon, A. Colin and P. D. Olmsted, *Phys. Rev. E: Stat., Nonlinear, Soft Matter Phys.*, 2010, **81**, 021502.
100 M.-A. Fardin, O. Radulescu, A. Morozov, O. Cardoso, J. Browaeys and S. Lerouge, *J. Rheol.*, 2015, **59**, 1335–1362.
101 H. Mohammadigoushki and S. J. Muller, *Soft Matter*, 2016, **12**, 1051–1061.
102 P. Cheng, M. C. Burroughs, L. Gary Leal and M. E. Helgeson, *Rheol. Acta*, 2017, **56**, 1007–1032.
103 S. Varchanis, A. Syrakos, Y. Dimakopoulos and J. Tsamopoulos, *J. Non-Newtonian Fluid Mech.*, 2020, **284**, 104365.
104 S. Varchanis and J. Tsamopoulos, *Sci. Talks*, 2022, **3**, 100053.
105 J. Adams, S. Fielding and P. Olmsted, *J. Non-Newtonian Fluid Mech.*, 2008, **151**, 101–118.
106 T. C. Papanastasiou, N. Malamataris and K. Ellwood, *Int. J. Numer. Methods Fluids*, 1992, **14**, 587–608.
107 E. J. Hinch, *J. Non-Newtonian Fluid Mech.*, 1993, **50**, 161–171.
108 E. J. Doedel, V. A. Romanov, R. C. Paffenroth, H. B. Keller, D. J. Dichmann, J. Galán-Vioque and A. Vanderbauwhede, *Int. J. Bifurcation Chaos*, 2007, **17**, 2625–2677.
109 S. Varchanis, Y. Dimakopoulos and J. Tsamopoulos, *Phys. Rev. Fluids*, 2017, **2**, 124001.
110 J.-F. Berret, in *Rheology of Wormlike Micelles: Equilibrium Properties and Shear Banding Transitions*, ed. R. G. Weiss and P. Terech, Springer, Netherlands, Dordrecht, 2006, pp. 667–720.
111 Y. T. Hu and A. Lips, *J. Rheol.*, 2005, **49**, 1001–1027.
112 E. Miller and J. P. Rothstein, *J. Non-Newtonian Fluid Mech.*, 2007, **143**, 22–37.
113 J.-B. Salmon, A. Colin, S. Manneville and F. Molino, *Phys. Rev. Lett.*, 2003, **90**, 228303.
114 P. D. Patil, J. J. Feng and S. G. Hatzikiriakos, *J. Non-Newtonian Fluid Mech.*, 2006, **139**, 44–53.
115 H. Giesekus, *Rheol. Acta*, 1962, **2**, 101–112.
116 R. J. Poole, *J. Non-Newtonian Fluid Mech.*, 2023, **320**, 105106.
117 G. H. McKinley, P. Pakdel and A. Öztekin, *J. Non-Newtonian Fluid Mech.*, 1996, **67**, 19–47.
118 B. Wojcik, J. LaRuez, M. Cromer and L. A. Villasmil Urdaneta, *Appl. Sci.*, 2021, **11**, 6588.
119 H. K. Moffatt, *J. Fluid Mech.*, 1964, **18**, 1–18.

 This journal is © The Royal Society of Chemistry 2024